Accepted Manuscript

Title: Density of states characterization of TiO_2 films deposited by pulsed laser deposition for heterojunction solar cells

Authors: Daniele Scirè, Roberto Macaluso, Mauro Mosca, Maria Pia Casaletto, Olindo Isabella, Miro Zeman, and Isodiana Crupi

DOI: https://doi.org/10.1007/s12274-021-3985-8

Published in: Nano Research

Received: 7 July 2021

Revised: 8 November 2021

Accepted: 9 November 2021

Published: 6 December 2021

Please cite this article as: Scirè D., Macaluso R., Mosca M, Casaletto M. P., Isabella O, Zeman M. and Crupi I. Density of states characterization of TiO_2 films deposited by pulsed laser deposition for heterojunction solar cells. Nano Research 2022 https://doi.org/10.1007/s12274-021-3985-8.

Nano Research

ISSN 1998-0124 CN 11-5974/O4
https://doi.org/(automatically inserted by the publisher)

Density of states characterization of TiO_2 films deposited by pulsed laser deposition for heterojunction solar cells

Daniele Scirè[1] (✉), Roberto Macaluso[1], Mauro Mosca[1], Maria Pia Casaletto[2], Olindo Isabella[3], Miro Zeman[3], and Isodiana Crupi[1]

[1] *Department of Engineering, University of Palermo, Viale delle Scienze, Ed. 9, Palermo, 90128, Italy*
[2] *Institute of Nanostructured Materials (ISMN), National Research Council (CNR), Via Ugo La Malfa 153, Palermo, 90146, Italy*
[3] *Photovoltaic Materials and Devices Group, Delft University of Technology, Mekelweg 4, Delft, 2628CD, the Netherlands*

Received: day month year / **Revised:** day month year / **Accepted:** day month year (automatically inserted by the publisher)

ABSTRACT

The application of titanium dioxide (TiO_2) in the photovoltaic field is gaining traction as this material can be deployed in doping-free heterojunction solar cells with the role of electron selective contact. For modeling-based optimization of such contact, knowledge of the titanium oxide defect density of states is crucial. In this paper, we report a method to extract the defect density through nondestructive optical measures, including the contribution given by small polaron optical transitions. The presence of both related to oxygen-vacancy defects and polarons is supported by the results of optical characterizations and the evaluation of previous observations resulting in a defect band fixed at 1 eV below the conduction band edge of the oxide. Solar cells employing pulsed laser deposited-TiO_2 electron selective contacts were fabricated and characterized. The J-V curve of these cells showed, however, a S-shape, then a detailed analysis of the reasons of such a behavior was carried out. We use a model involving the series of a standard cell equivalent circuit with a Schottky junction in order to explain these atypical performances. A good matching between the experimental measurements and the adopted theoretical model was obtained. The extracted parameters are listed and analyzed to shade light on the reasons behind the low-performance cells.

KEYWORDS

solar cell, heterojunction, photovoltaic, defect density, small polaron, Pulsed Laser Deposition, titanium dioxide, defects

1. Introduction

The rise in renewable energy production from solar irradiation has led to rapid growth in the photovoltaic market, with the solar PV module industry gaining considerable traction as the silicon-based technology reached about the 95% of the total production in 2019 and the crystalline-silicon (c-Si) technology 66% of total production [1]. Indeed, the c-Si heterojunction technology (HJT) represents an interesting innovation leading to solar cells with record efficiency over 26% [2,3] and at industrial level of 24.63% [4]. Such results were achieved thanks to the excellent passivation properties of the hydrogenated amorphous silicon (a-Si:H) [5]; despite these achievements, exploiting a-Si:H introduces some drawbacks due to the large presence of defects and parasitic absorption [6], moreover, the further optimization of the hydrogenated amorphous silicon layer is challenging [7]. Therefore, other materials such as the transition metal oxides (TMOs) are currently investigated to replace a-Si:H in HJT and implement passivating carrier selective contacts (CSC) [8]. These contacts are typically made of TMOs like TiO_2, ZnO and TaO (for the electron selective contact) [9–11], MoO_3, WO_3 and V_2O_5 (for the hole selective contact) [12–14] and can be deposited reliably with a variety of different techniques such as atomic layer deposition, atmospheric pressure chemical vapor deposition, physical vapor deposition and wet chemical methods [15]. Examples of HJT cells implementing TMOs selective contacts have been reported [7,16–18], reaching efficiency up to 23.5% [19]. For the electron selective contact, titanium dioxide in its sub-stoichiometric form (TiO_x) (x <2) represents a suitable choice. Indeed, such material presents at the interface with the n-type silicon a large offset in the valence band, forming a barrier that blocks the hole transport; at the same time, it presents a good alignment of the conduction bands with a small offset, allowing the electrons to pass through the selective contact [18,20]. Nonetheless, TiO_x can also act as a hole selective contact depending on the deposition process [21], with its carrier selectivity property strongly influenced by the post-deposition annealing, plasma treatment, work-function of the capping layer, and TiO_x thickness [21].

The formation of the sub-stoichiometric TiO_x compound is essential to achieve adequate selectivity and passivation. The presence of oxygen vacancies is necessary for achieving a low contact resistivity; in fact, the film conductivity increases as the oxygen vacancies increment provides *n*-type doping [22].

TiO_x is one of the most employed TMOs as an electron selective contact, with several studies highlighting its characteristics,

Address correspondence to daniele.scire@unipa.it

implementing them in HJT [9,23,24] and reaching efficiency over 22% [25], and a significative efficiency of 21.8% when contacted with a low work function metal such as calcium [26]. Moreover, titanium dioxide has a role in the enhancement of the characteristics of perovskite solar cells [27,28]. Although this transition metal oxide was previously studied and characterized for various electronic devices [29–32], its performances in heterojunction solar cells are currently under a process of optimization. Thus, gaining insight into the role of the bandgap defects related to the oxygen vacancies is of particular importance [33,34], since these defect states actively contribute to the carrier transport in TMOs-based cells [35]. Indeed, lack of information on the defect density of states of TMO layers may compromise any optimization of such solar cell architecture leading to sub-optimal DC characteristics with S-shaped J–V curves [14], with a considerable decrease in the cell electrical performances.

Furthermore, the lack of detailed knowledge of the interface defect parameters limits the accuracy of the model of the tunneling mechanism due to defects in the junction between p-Si and TiO_2 in monolithic perovskite/Si tandem cells [36]. Nonetheless, a quantitative study on the defect density of states in the bandgap of the TiO_x for solar cells devices has not yet proposed. For these reasons, in order to avoid the undesired S-shaped current behavior of solar cells, it is essential to shade light to material's properties that may be responsible for these low performance devices.

The defect density of states of a thin film can be extrapolated from its absorption coefficient and by evaluating the optical transitions between available states and the conduction band. For this purpose, an absolute photothermal deflection spectroscopy (PDS) setup has been used to measure optical transmittance , reflectance and absorptance values in a wide spectral range [23,24] simultaneously; such technique has been extensively used to achieve information on the defectivity of semiconductors [37–39]. Furthermore, the contribution to the absorption coefficient due to the small polaron has also been considered; such technique was previously used for characterizing the sub-gap defect density in transition metal oxides such as molybdenum oxide [40,41].

2. Methodology

Layers of titanium oxide 150 nm-thick were deposited by Pulsed Laser Deposition (PLD) on quartz substrates from a TiO_2 (Balzers, 99.5%) target. Depositions were carried out at two different temperatures (room temperature and 200 °C) and under three different oxygen pressures (PO_2) such as 2×10^{-2}, 1×10^{-2} and 1×10^{-3} mbar. Three additional samples were prepared in vacuum ambient (at room temperature and 200 °C) and at an oxygen pressure of 1×10^{-2} mbar (at 400 °C) for comparison purposes. Films thickness was assessed by spectroscopic ellipsometry (SE) with a single Cody-Lorentz oscillator [29]. The mean thickness resulted 155 nm with a small variation among the samples deposited in oxidating ambiance at room temperature and at 200 °C, whereas the TiO_x film deposited at 400 °C resulted thinner (35 nm) and the samples prepared in vacuum presented a film thickness of 113 nm (at room temperature) and 95 nm (at 200 °C).

X-Ray Photoemission Spectroscopy (XPS) was used to investigate the electronic structure of TiO_2 samples and to determine the surface relative chemical composition. Films in the 'as received' condition were submitted to XPS analysis with no additional pre-treatment prior measurements.

Samples were analyzed by means of a VG MicrotechESCA3000 Multilab spectrometer, equipped with an ultrahigh vacuum chamber (base pressure $< 1 \times 10^{-6}$ Pa); a twin (Mg and Al) anode as X-Ray source and a five channeltrons detection system. XPS spectra were acquired using a standard non-monochromatized Al K_α (hν= 1486.6 eV) excitation source and a hemispherical analyser operating in CAE mode. VGX900 and XPSPEAK4.1 software were used for the collection and processing of photoemission spectra, respectively. The binding energy (BE) scale was charge corrected by using C 1s peak (BE = 285.1 eV) from the adventitious carbon on the surface. The accuracy of the binding energy measure is ± 0.1 eV. The chemical shift of XPS signals was determined by a nonlinear least square curve-fitting procedure, using a properly weighted sum of Lorentzian and Gaussian component for the shape of Voight curves and a Shirley background subtraction [42]. The surface chemical composition, expressed as relative atomic percentage, was obtained by a standard quantification routine, including Wagner's energy dependence of attenuation length [43] and a standard set of VG Escalab sensitivity factors. The uncertainty on the atomic quantitative analysis is ± 10%. Photoelectron signals and peak components were assigned according to XPS literature reference database [44].

The morphological evaluation of the TiO_x layers has been investigated by Raman spectroscopy (λ=514 nm) performed with a Renishaw inVia Micro-Raman microscope. The absorption coefficient of the samples was measured by a PDS setup which is described elsewhere [45,46].

The solar cell prototype was fabricated following the process described in [47] in which a c-Si solar cell uses a stack of intrinsic hydrogenated amorphous silicon, doped hydrogenated nanocrystalline silicon oxide (nc-SiO_x:H) and doped hydrogenated nanocrystalline silicon (nc-Si:H). The absorber is an n-type <111> oriented c-Si wafer (280 µm-thick, resistivity of 2.5 Ω·cm and doping concentration of 1.9×10^{15} cm^{-3}). The p-contact was formed by Plasma Enhanced Chemical Vapor Deposition (PECVD) with a stack of 9 nm a-Si:H(i), 10 nm of nc-SiO_x:H(p) and 10 nm of nc-Si:H(p); the n-contact was prepared with a passivation layer of 9 nm of a-Si:H(i). A square of 1.5 cm×1.5 cm was obtained after the dicing of the wafer and used for the electron selective contact deposition of 5 nm of TiO_2 by Pulsed Laser Deposition (PLD) onto the passivation layer. The prototypes were finalized by sputtering of indium tin oxide (ITO) as an anti-reflecting coating (70 nm on the front side, 140 nm on the backside) while metallization was obtained by thermal evaporation of 1 µm-thick aluminum layer on both faces of the devices. In particular, the bottom contact was obtained with a full Al deposition onto the TiO_x film, while the top contact was deposited onto the ITO film through a shadow mask with a grid pattern.

A sketch of the solar cell prototype is depicted in Figure 1, showing the hole selective contact made with a stack of doped hydrogenated nanocrystalline silicon oxide and the electron selective contact made with the titania film.

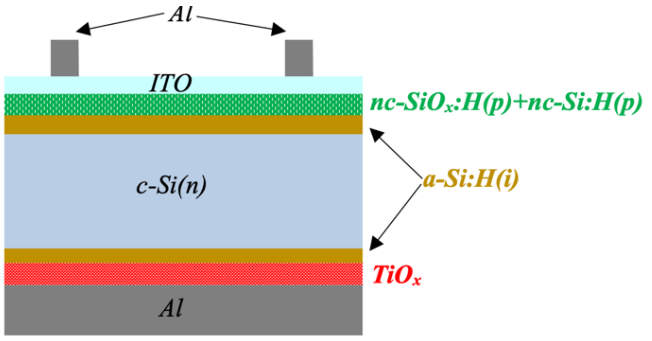

Figure 1 Sketch of the solar cell prototype exploiting titanium dioxide as electron selective contact

3. Results and discussion

3.1 Chemical and structural characterization

The surface composition of the deposited films was analyzed by X-ray photoemission spectroscopy (XPS). Ti 2p spectra shown in Fig. 2 refer to the samples deposited at ambient temperature with a partial pressure of oxygen PO_2 of 1×10^{-3} mbar (Fig. 2(a)) and 2×10^{-2} mbar (Fig. 2(b)), respectively. The presence of a doublet peak with the Ti $2p_{3/2}$ located at BE = 458.6 eV and Ti $2p_{1/2}$ at BE = 464.4 eV is assigned to Ti^{4+} oxidation state, which corresponds to the TiO_2 compound [48,49].

The curve-fitting of O 1s spectra is reported in Fig. 3(a) for the sample deposited at $PO_2=1\times10^{-3}$ mbar, and in Fig. 3(b) for the sample deposited at $PO_2=2\times10^{-2}$ mbar, respectively. Results are summarized in Table 1. The two different components located at BE = 530.0 eV and at BE = 531.4 eV correspond to oxides and defective oxides or adsorbed hydroxyl species, respectively [49]. The evidence that both the samples are sub-stochiometric is confirmed by the relative chemical composition of the surface listed in Table 2. Ti 2p and O 1s photoelectron signals can be used in combination to determine the stoichiometry of the TiO_2 films. For the determination of the O/Ti atomic ratio, the contribution of the –OH component resulting from the curve-fitting of the O 1s peak with two components can be neglected in the calculation [50]. Results are reported in Table 2 for the detected O/Ti and calculated O/Ti^* ratio. The surface relative chemical composition determined by XPS confirmed that TiO_2 is sub-stochiometric in both the investigated films.

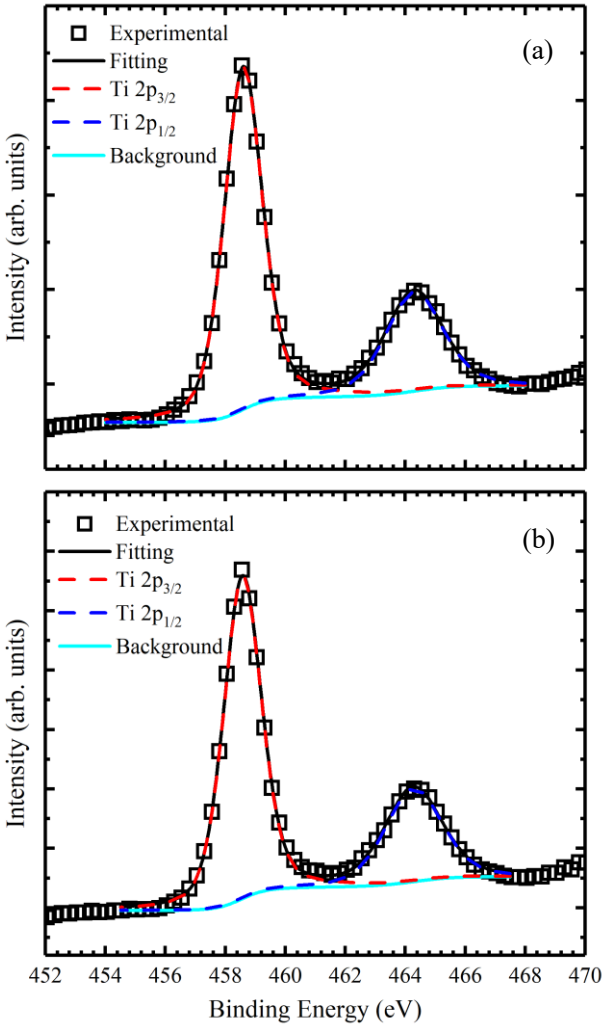

Figure 2 Curve fitting of Ti 2p spectra for TiO_2 films deposited at: (a)$PO_2 = 1\times10^{-3}$ mbar , (b) $PO_2 = 2\times10^{-2}$ mbar.

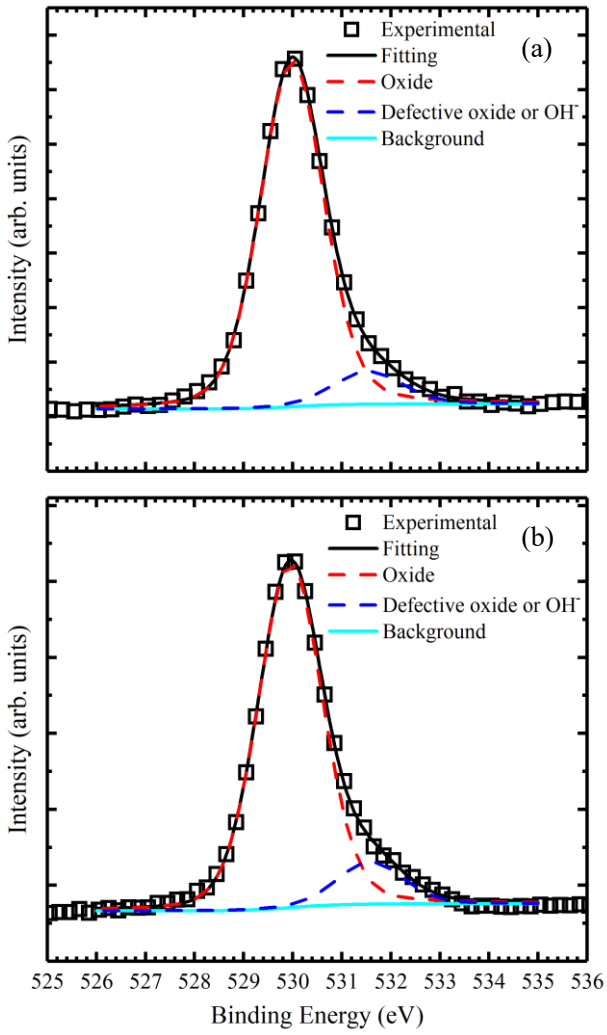

Figure 3 Curve fitting of O 1s spectra for TiO_2 films deposited at: (a) $PO_2 = 1\times10^{-3}$ mbar , (b) $PO_2 = 2\times10^{-2}$ mbar.

Table 1. XPS results of Ti 2p and O 1s curve-fitting in the investigated samples. The two spin-orbit components ($2p_{3/2}$ and $2p_{1/2}$) of Ti 2p spectrum resulted energy split by Δ_{oxide}=5.7 eV.

PO_2 (mbar)	*XPS signal*	*BE* (eV)	*Peak area* (%)
1×10^{-3}	Ti $2p_{3/2}$	458.6	100
1×10^{-3}	O 1s	530.0	90.6
		531.5	9.4
2×10^{-2}	Ti $2p_{3/2}$	458.6	100
2×10^{-2}	O 1s	530.0	88.8
		531.6	11.2

Table 2. XPS surface relative chemical composition in the investigated samples. Elemental concentration is expressed as atomic percentage (at. %). The O/Ti* ratio was calculated after removing the contribution of the –OH component from the O 1s peak.

PO_2 (mbar)	*Ti 2p* (%)	*O 1s* (%)	*O/Ti*	*O/Ti*$^+$
1×10^{-3}	34.3	65.7	1.9	1.7
2×10^{-2}	36.9	63.1	1.7	1.5

Structure and composition of the deposited oxides was analyzed by evaluating the Raman spectrum. The results are highlighted in Fig. 4; in particular, Fig. 4(a) shows the Raman spectra for the samples prepared with PO_2 equal to 1×10^{-3} mbar and 2×10^{-2} mbar at ambient temperature and 200 °C. Similar behavior was measured for the samples obtained with PO_2=1×10^{-2} mbar (not reported here). No sharp peaks are observed in the spectra, confirming that the material is amorphous even when deposited at 200°C. Indeed, a higher temperature is required to start crystallization [51–55]. For comparison purposes, Fig. 4(b) shows the Raman spectrum of a TiO_x sample deposited at 400°C with PO_2=1×10^{-2} mbar in which the presence of sharp peaks (145, 198, 399, 516, 640 cm^{-1}) is highlighted; such peaks are correlated to the anatase crystalline phase [56,57].

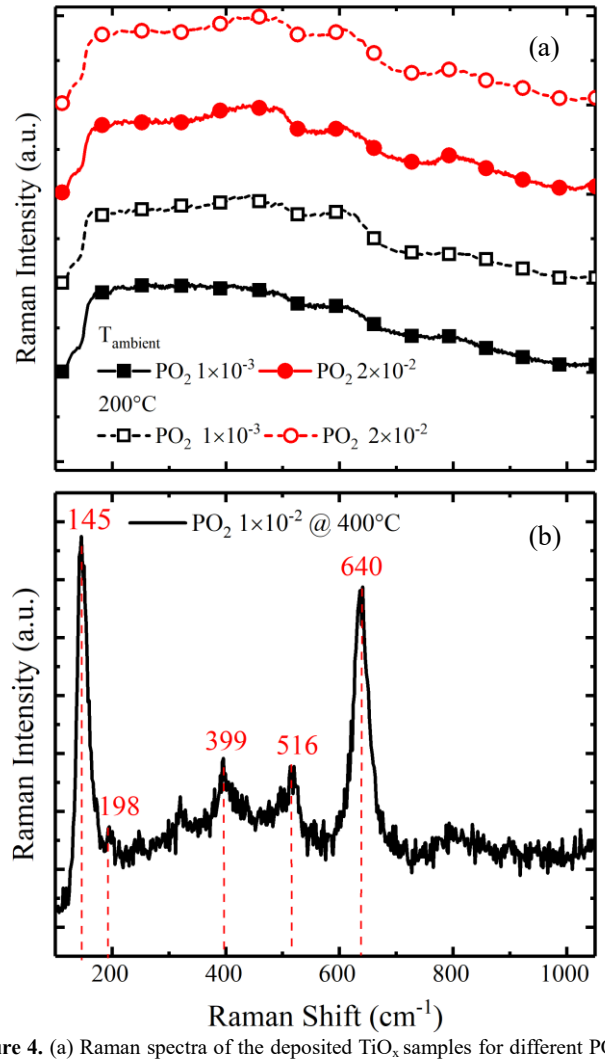

Figure 4. (a) Raman spectra of the deposited TiO_x samples for different PO_2 and deposition temperature; (b) Raman spectrum of the TiO_x sample deposited at 400°C with PO_2=1×10^{-2} mbar.

3.2 Optical characterization

The optical absorption spectra of the TiO_x samples are shown in Fig. 5. As a reference, we report the spectra of the films deposited in vacuum ambient (e.g., without introducing oxygen within the PLD deposition chamber) at ambient temperature and 200 °C. The spectra of these two samples are similar, meaning that the absorption coefficient ($\alpha \approx 10^5$ cm^{-1}) is almost constant throughout the whole measurement range. It should be noted that the deposition of the films in the absence of O_2 led to very different samples with opaque-black coloration and a high absorption spectrum (Fig. 5); such behavior is typical of the *black-TiO_2* [58,59] and is caused by a large defect concentration due to the oxygen vacancies.

The other samples, prepared in a O_2 environment, present a similar trend of the absorption in accordance with previous observations [60]. Each spectrum increases from lower energies to a small, broad peak in the region located around 1.4 eV; it then decreases to a lower value at 3 eV and then rises up again exponentially. From 1 eV to 3 eV, the absorption spectra of the films deposited at ambient temperature are slightly higher than the ones deposited with the same PO_2 at 200°C. The sample deposited with PO_2=1×10^{-3} mbar at 200°C exhibits significantly lower absorption than the sample deposited for the same oxygen pressure at ambient temperature.

This behavior can be attributed to a less defective lattice than the materials deposited at ambient temperature, giving a minor oxygen vacancy content, which leads to a lower absorption coefficient. In the 3-4 eV range, the absorption coefficient of the samples deposited at 200°C is slightly lower than the sample obtained at ambient temperature, regardless of the oxygen pressure used. Finally, as a general trend, the higher is the oxygen pressure, the lower is the absorption coefficient. A minor content of oxygen vacancies in the lattice can explain this behavior; indeed, the higher PO_2 improves the stoichiometric ratio of the compound [61], reducing the defects due to the oxygen vacancies, thus reducing the absorption.

The optical band gaps, E_{opt}, of the samples were evaluated by Tauc's law [62]:

$$(\alpha h\nu)^{\frac{1}{n}} \propto (h\nu - E_{opt}) \quad (1)$$

where $h\nu$ is the photon energy and n is equal to ½ for the direct allowed transition.

The resulting values are summarized in Table 3 and range between 3.31 and 3.38 eV. This means that there is a slight difference between the optical band gap values, with the film deposited at the highest oxygen pressure (PO_2=2×10^{-2} mbar) exhibiting the largest optical band gap deviation from the other samples.

The Urbach energy, E_U of the samples was evaluated using Urbach's relation (2) [63] and the results are reported in Table 3.

$$\alpha \propto \exp\left(\frac{h\nu}{E_U}\right) \quad (2)$$

Under the same oxygen pressure conditions, the samples grown at ambient temperature are characterized by a higher E_U with respect to the ones deposited at 200 °C. The increase in Urbach's energy and the narrowing of the optical gap can be related to the increased defect density induced by the oxygen vacancies in the oxide film [64,65].

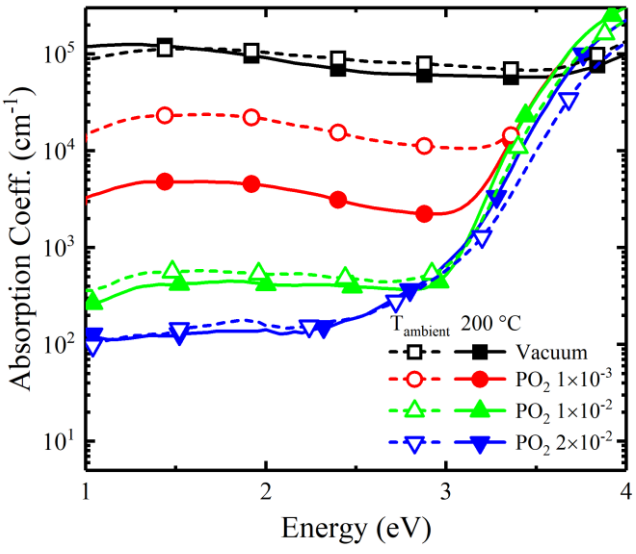

Figure 5 Absorption spectra for TiO_x samples deposited at different conditions of temperature and pressure (expressed in mbar)

Table 3. Tauc Gap, E_{opt}, and Urbach Energy, E_U, evaluation

PO_2 (mbar)	*Temperature* (°C)	E_{opt} (eV)	E_U (meV)
1×10^{-3}	Amb.	3.31	185
1×10^{-3}	200°C	3.31	143
1×10^{-2}	Amb.	3.32	124
1×10^{-2}	200°C	3.30	110
2×10^{-2}	Amb.	3.38	142
2×10^{-2}	200°C	3.34	131

3.3 Density of States extrapolation

The density of states (DOS) can be described as the superposition of different elements assuming a parabolic distribution for the valence and conduction bands (N_{VB}, N_{CB}), an exponential distribution for the valence and conduction band tails (N_{VBT}, N_{CBT}), and a Gaussian distribution for the defects states in the bandgap (N_D) [40,66].

$$DOS(E) \rightarrow \begin{cases} N_{VB}(E) = N_V\sqrt{-E + E_G + E_{0V}} & E < 0 \\ N_{CB}(E) = N_C\sqrt{E - E_{0C}} & E \geq 0 \\ N_{VBT}(E) = N_V\sqrt{\frac{E_{0V}}{2}}\exp\left(-\frac{E+E_G}{E_{0V}}\right) & E > E_G \\ N_{CBT}(E) = N_C\sqrt{\frac{E_{0C}}{2}}\exp\left(\frac{E}{E_{0C}}\right) & E < 0 \\ N_D(E) = \frac{A_D}{\sqrt{2\pi W_D^2}}\exp\left[-\frac{1}{2}\left(\frac{E+E_D}{W_D}\right)^2\right] & E_G < E < 0 \end{cases} \quad (3)$$

Considering the zero-energy reference level at the edge of the conduction band, N_V = 7.09·10^{19} cm^{-3}eV$^{-3/2}$ and N_C = 6.77·10^{20} cm^{-3}eV$^{-3/2}$ are the DOS of the valence and conduction band, respectively. These values have been calculated considering the values of the effective masses for electrons and holes reported in [67]. E_{0V} and E_{0C} are the slopes of the valence and conduction band tails, and E_G is the energy gap. The inter-bands defects are modeled with a Gaussian distribution defined by the mean energy position of the defects E_D (which reflects the distance of the defect distribution from the conduction band edge) and the full width at half maximum (FWHM) W_D. With this model, the Gaussian distribution is normalized; therefore, to fit this distribution with the experimental data, a multiplicative term A_D [eV^{-1}cm^{-3}] is introduced, the area of the defect density of states. The number of defect states at a specific energy [cm^{-3}] in the bandgap is obtained by evaluating N_D at the desired energy. As such, the defect area A_D is directly proportional to the number of trap states for a cm^3.

The absorption spectra α($h\nu$) could be modeled by the *one-electron approximation* [38]:

$$\alpha(h\nu) = \frac{C}{h\nu}\int N_i(E)F(E)N_f(E+h\nu)[1-F(E+h\nu)]dE \quad (4)$$

where $h\nu$ is the photon energy, C is a parameter which depends on both the refractive index and the momentum matrix elements and is assumed constant for all the optical transitions [38,66,68], $N_i(E)$ is the density of the initial occupied states, $N_f(E)$ is the density of final empty states, while $F(E)$ is the Fermi-Dirac function. However, since the absorption spectra of the TiO_x samples shows a peak in the sub-gap absorption region, the one-electron approximation is not suitable for this analysis and an extension of this model is needed by introducing an additive term modeling the absorption due to the small polarons [40,41], which is a quasi-particle used to model the interaction of trapped electrons with the surrounding atoms [69,70] and is responsible for the peak in the NIR region of the absorption spectrum [71–73]; furthermore, the presence of the small polarons has been previously evaluated in TiO_2 [74–76] and in other TMOs [71,75,77,78]. The small polarons give a contribution to the absorption modeled as a weakly asymmetric Gaussian peak [71,72] with A_p pre-exponential factor, E_p polaron binding energy and E_{op} longitudinal-optical phonon energy:

$$\alpha_p(h\nu) = \frac{A_p}{h\nu}\exp\left(-\frac{(h\nu - 2E_p)^2}{8E_p\,E_{op}}\right) \quad (5)$$

Introducing the polaron contribution in (4) gives the following equation:

$$\alpha(h\nu) = \frac{C}{h\nu}\int N_i(E)F(E)N_f(E+h\nu)[1-F(E+h\nu)]dE + \frac{A_p}{h\nu}\exp\left(-\frac{(h\nu - 2E_p)^2}{8E_p\,E_{op}}\right) \quad (6)$$

The constant C was evaluated for each spectrum from (6) by calculating it at 4 eV. It should be noted that, at this energy, the optical transition from the valence to the conduction band gives the most prominent contribution to the absorption; therefore, only this contribution is considered for the constant calculation. The resulting C values lay within the range (1.11-2.02)×10^{-34} cm^5·eV^2 and are listed in Table 4.

Table 4. Constant C values for different deposition conditions

PO_2 (mbar)	*Temperature* (°C)	C (cm^5·eV^2)
1×10^{-3}	Ambient	1.31×10^{-34}
1×10^{-3}	200°C	2.02×10^{-34}
1×10^{-2}	Ambient	1.13×10^{-34}
1×10^{-2}	200°C	1.37×10^{-34}
2×10^{-2}	Ambient	1.11×10^{-34}
2×10^{-2}	200°C	1.18×10^{-34}

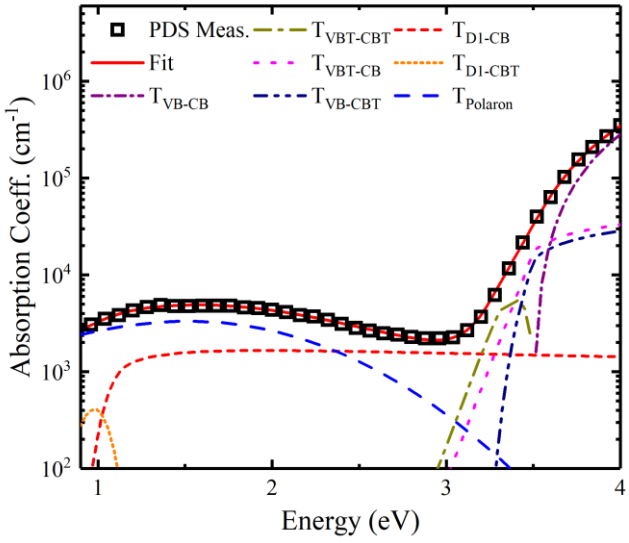

Figure 6 Absorption spectrum deconvolution for the TiO_x film deposited at PO_2=1×10^{-3} mbar and 200 °C.

Figure 6 presents an example of the absorption fit for the sample prepared with PO_2=1×10^{-3} mbar at 200 °C. The absorption spectrum is composed of many elements representing the contribution due to the optical transitions from the valence to the conduction band ($T_{VB\text{-}CB}$): from the valence band tail to the conduction band tail ($T_{VBT\text{-}CBT}$); from the valence band tail to the conduction band ($T_{VBT\text{-}CB}$); from the valence band to the conduction band tail ($T_{VB\text{-}CBT}$); from the inter-band defects to the conduction band ($T_{D\text{-}CB}$); from the defects in the bandgap to the conduction band tail ($T_{D\text{-}CBT}$), and finally to the transition due to the polaron ($T_{Polaron}$).

The parameters obtained by the deconvolution of the absorption spectra are listed in Table 5 and are related to the layers of titanium dioxide deposited with PO_2 of 1×10^{-3}, 1×10^{-2} and 2×10^{-2} mbar at ambient temperature and 200 °C.

It is worth pointing out that E_{0V} of the samples deposited at ambient temperature is always higher than the samples deposited at the same oxygen pressure and 200 °C; a different trend is reported for E_{0C}, which for the samples prepared at ambient temperature is lower than the samples deposited with the same PO_2 at 200 °C. These results are consistent with the Urbach energy reported in Table 3; indeed the Urbach energy is a measure of the disorder and the defectivity of the material and is related to the slope of extended tails in the valence and conduction band [79]. For the defects distribution in the bandgap, E_D ranges around a mean value of 1 eV below the conduction band edge, with standard deviations varying from 50 to 80 meV.

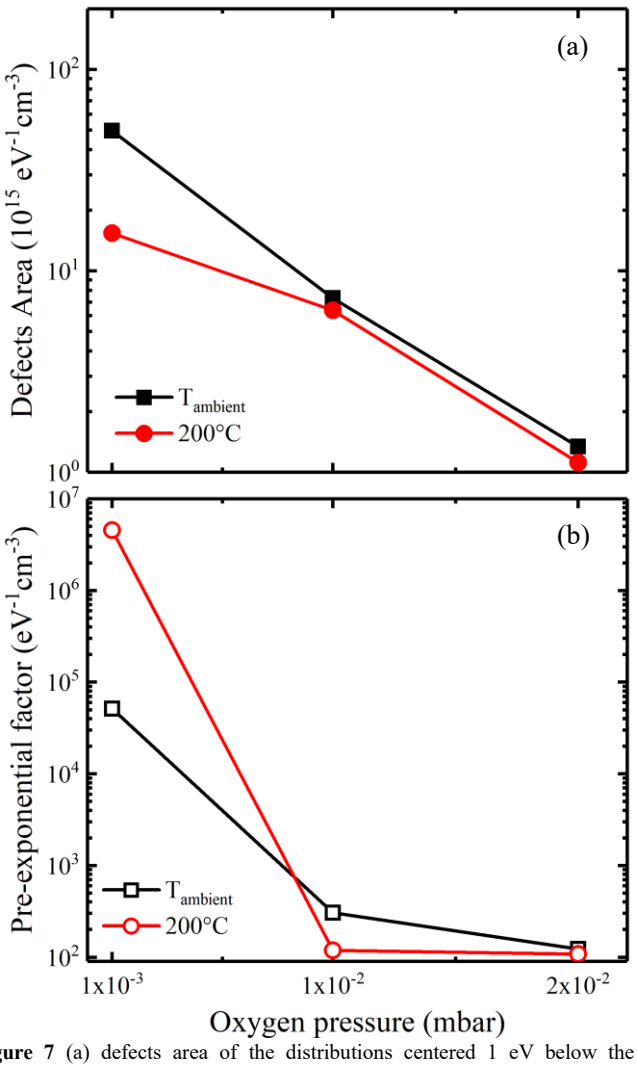

Figure 7 (a) defects area of the distributions centered 1 eV below the conduction band and (b) pre-exponential factor of the polaron absorption as a function of the oxygen deposition pressure at ambient temperature and 200 °C.

The electronic states of defects are spatially localized and energetically positioned within the bandgap. The energy position value agrees with other results reporting a localized oxygen vacancy in TiO_x at about 1 eV below the conduction band [74,76,80]. The localization energy of these states is fixed since it is directly related to the chemical nature of such defects [81]. Moreover, , a theoretical study has shown that the energy position of the defect states can be tuned by doping the TiO_2 with 3d transition metal-oxides [82]. Such a study highlighted that as the atomic number of the dopant increased, the localized level shifted to lower energy.

The defects area shows a significant trend with both deposition temperature and pressure. In particular, as shown in Fig. 5, the raise of the deposition temperature reduces the value of A_D regardless of the used oxygen pressure. However, this effect is more evident for the sample deposited at 1×10^{-3} mbar and T_{amb}, which presents a defects area roughly three times larger than for the samples prepared at 200 °C.

Fig. 7(a) shows that the A_D values decrease with the oxygen pressure for both deposition temperatures. As a consequence, one can say that the deposition of these oxides in a high oxygen-content environment reduces the formation of oxygen vacancies; furthermore, this effect is enhanced by a high deposition temperature.

Table 5 The density of states and small polaron parameters for different deposition conditions.

PO_2 (mbar)	*Temp* (°C)	E_{0V} (meV)	E_{0C} (meV)	A_D (ev^{-1}cm^{-3})	E_D (eV)	W_D (eV)	A_P (ev^{-1}cm^{-3})	E_P (eV)	E_{op} (meV)
1×10^{-3}	Amb.	136	609	4.96×10^{16}	1.02	0.08	5.17×10^{4}	0.94	86.41
1×10^{-3}	200°C	128	628	1.54×10^{16}	1.05	0.06	4.58×10^{6}	0.93	117.10
1×10^{-2}	Amb.	114	585	7.33×10^{15}	1.05	0.08	3.05×10^{2}	0.91	105.60
1×10^{-2}	200°C	104	568	6.37×10^{15}	1	0.08	1.19×10^{2}	0.93	110.11
2×10^{-2}	Amb.	136	592	1.34×10^{15}	1.05	0.05	1.23×10^{2}	0.94	112.37
2×10^{-2}	200°C	130	602	1.12×10^{15}	1.08	0.08	1.08×10^{2}	0.94	120.03

Figure 7(b) also shows the data extrapolated from the fitting relative to the pre-exponential factor of the polaron absorption, which presents a similar trend to the defects area with a descending A_p for both increasing deposition oxygen pressure and temperature; furthermore, at 1×10^{-3} mbar the film deposited at 200 °C presented a much larger pre-exponential factor. Finally, E_P results unchanged by the deposition conditions, with mean value 0.93 eV; E_{op}, instead, fluctuates between 86 and 120 meV with mean value of 113.4 eV.

3.4 Application in c-Si heterojunction solar cell

The energy band diagram of a cell exploiting titania as electron selective contact is sketched in Figure 8. The defects states in the forbidden band of the TiO_x close to the conduction and valence bands (extended states or band-tails with blue dots) and the defects localized at 1 eV below the conduction band edge (red stripes) are represented. The arrows represent the flow of the carriers through the heterojunction (full circles for the electrons and void circles for the holes). The heterojunction c Si(n)/a-Si:H(i)/TiO_x provides an electron selective contact repelling the holes with an energy barrier in the valence band while it shows a viable path for the electron flow through tunneling mechanism such as *the direct tunneling* and the *trap-assisted tunneling*.

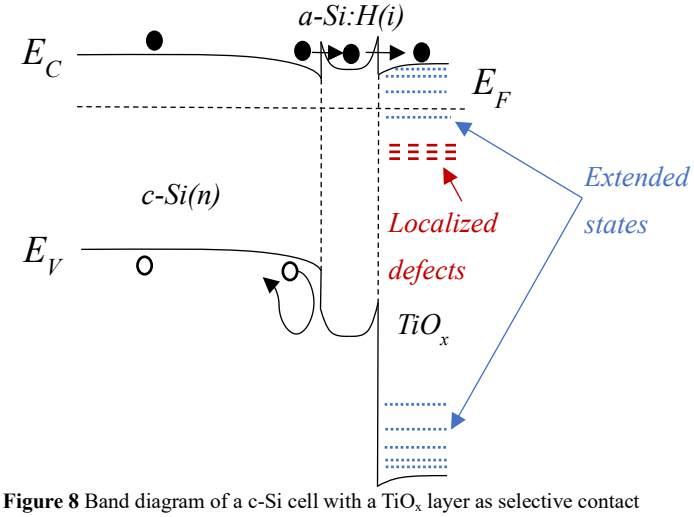

Figure 8 Band diagram of a c-Si cell with a TiO_x layer as selective contact

Figure 9(a) presents the experimental *J-V* curve characteristics under AM 1.5 illumination for the heterojunction solar cells realized using a film of TiO_x as electron selective carrier contacts. The oxide layer was deposited with $PO_2=1\times10^{-3}$ mbar at ambient temperature. The measurement shows an S-shaped *J-V* characteristic, a phenomenon associated with a barrier for electron transport through the TiO_x layer due to the mismatch between the work functions of the TiO_x and the passivation layer. The presence of such a barrier has been reported in refs. [83,84] likely caused by the non-optimal alignment of the band structure in the cell, particularly between the layers of the carrier selective contact and the a-Si:H(i).Therefore, optimizing the titanium oxide deposition is needed to improve the DC characteristic of any solar cells exploiting TiO_x carrier selective contact. Indeed, the properties of transition metal oxides, such as optical band gap, work function, crystallinity and stoichiometry, depend on the deposition technique, the substrate temperature and the deposition oxygen pressure. For this purpose, the current density-voltage curve information is useful to increase awareness regarding the use of TiO_x as carrier selective contact in heterojunction solar cells technology. Such information can be extrapolated from the parameters of the DC model of the solar cell. Several model have been validated for the solar cells for static and dynamic behavior [85]; however, the S-shape *J-V* characteristic cannot be explained with a standard model and therefore, a more complex model has been proposed [86,87] modeling the barrier as shown in Fig. 9(b) with a rectifying Schottky junction connected in series with the heterojunction cell top model as in [88] and applied previously to solar cells with TMO-based hole-selective contact [13]. Hence, the model, represented in Fig. 9(b), is described by the equations (7-9), with the following parameters for the heterojunction: J current density, V_1 bias voltage, J_{PH} photogenerated current density, J_{01} leakage current density, n_1 ideal factor of the diode, V_T thermal voltage (about 0.02585 V at 300 K), R_{S1} series resistance, R_{P1} shunt resistance, V_2 is the bias voltage; and for the rectifying junction: J_{02} leakage current density, n_2 ideal factor of the diode and R_{P2} shunt resistance.

$$J = J_{01}\left(exp\left(\frac{V_1 - JR_{S1}}{n_1 V_T}\right) - 1\right) + \frac{V_1 - JR_{S1}}{R_{P1}} - J_{PH} \quad (7)$$

$$J = J_{02}\left(exp\left(\frac{V_2}{n_2 V_T}\right) - 1\right) + \frac{V_2}{R_{P2}} \quad (8)$$

$$V = V_1 + V_2 \quad (9)$$

It should be remarked that the current density J is the same for both heterojunction and rectifying junction while the applied bias voltage V is split among the junctions. To evaluate (7), an expression of V_2 was obtained through the Lambert W function [89] providing a direct expression as in (9).

$$V_2 = R_{P2}(J_{02} + J) + n_2 V_T\, W\left(\frac{J_{02}R_{P2}}{n_2 V_T} exp\left(\frac{R_{P2}(J_{02} + J)}{n_2 V_T}\right)\right) \quad (10)$$

The DC model parameters of the solar cell device were obtained through a fitting procedure of (7, 9, 10) with the experimental *J-V* curve. The result of this procedure is shown in Fig. 8 where a good fitting of the model with the experimental data is highlighted in the entire voltage range. Moreover, the extrapolated cell parameters are listed in Table 6.

The large ideality factor n_2 of the Schottky diode means that the effective recombination lifetime in the depletion layer increases with an increasing recombination rate. Many interpretations of large ideality factors exist and are based on trap-assisted tunneling or field-enhanced recombination via single levels or even flowing at the edge of the diode and in certain shunt positions [90]. The presence of a large concentration of defects in the TiO_x layer allows for transport mechanisms such as trap-assisted tunneling which could increase the recombination current and rise the ideality factor of this Schottky contact.

The characteristic shown in Figure 10 gives an insight into the capabilities of the TiO_x-based solar cells, since it excludes the negative effect introduced by the Schottky junction. It is obtained considering only the HJT section of Fig. 9(b) (i.e., calculating (7), nulling the contribution of the rectifying junction, setting V_2 to zero). Results show that the HJT curves and the experimental ones share the same open-circuit voltage V_{OC}. Indeed, at open-circuit voltage, the current density in the whole device is null and the total bias voltage is therefore provided by the heterojunction section of the model (Fig. 9(b)) since the open-circuit voltage generation is independent of the Schottky junction. It is worth noting that, for voltages close to V_{OC}, the slope of the *J-V* curve is different for the two curves of Figure 10; this effect relies on the differential conductance of the device which, for the device with the S-shape, is dominated by the conductance of the rectifying junction at the open-circuit voltage ($1/R_{P2}$), that is much lower than the differential conductance of the heterojunction ($1/R_{P1}$) and is the reason for the formation of the S-shaped characteristic. For bias voltage higher than the open-circuit value, D_2 begin to conduct shortening R_{P2} and the *J-V* curve slope is dominated by the conductance ($1/R_{P1}$) as in the HJT simulated cell. Finally, for bias voltages lower than V_{OC}, the current density of the solar cell device is lower (for the same voltage) than the one obtained considering only the model parameters of the HJT cell reducing the fill factor. As the bias voltage further decreases, the photogenerated current density is dominant and the current density reaches its minimum value, which is equal to the solar cell prototype and the one simulated without the Schottky barrier.

Although the solar cell prototype shows low performances, the data presented in this study can be used in an advanced semiconductor simulator to optimize the next solar cells. One crucial aspect that needs to be examined in future studies is, indeed, the role of the thickness of the titania film. The presence of a Schottky barrier (which degraded the performance of the device) can be overcome by improving the conductivity of the carrier selective contact and reducing its thickness. Another possible approach is inserting a thin layer of a low work function metal, i.e., calcium, between the TiO_2 and the back metallization, forming the so-called ATOM contact [9]. This approach may be applied to improve the performance of the titania layers reducing the optoelectrical losses.

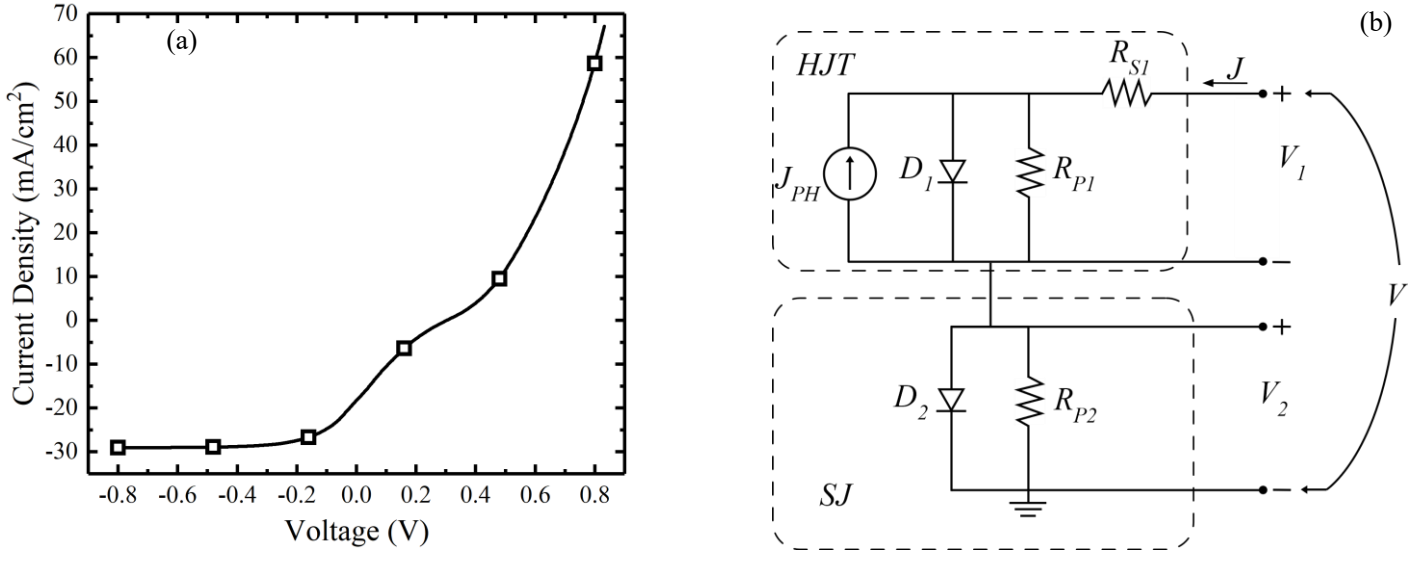

Figure 9 (a) Experimental J-V curve for a solar cell exploiting a TiO_x film as electron selective contact;(b) equivalent circuit of a heterojunction solar cell with a series Schottky junction.

Table 6. The equivalent circuit model parameters.

	Heterojunction				***Schottky Junction***			
PO_2 *(mbar)*	J_{01} (A/cm^2)	R_{S1} (Ω·cm^2)	R_{P1} (Ω·cm^2)	N_1	J_{PH} (A/cm^2)	J_{02} (A/cm^2)	R_{P2} (Ω·cm^2)	N_2
1×10^{-3}	1.15×10^{-4}	4.38	1000	1.68	2.83×10^{-2}	1.92×10^{-4}	5.50	2.70

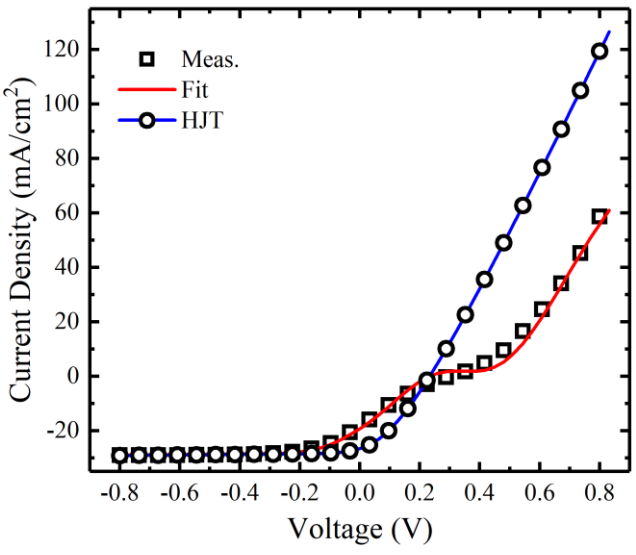

Figure 10 Experimental J-V curve of a heterojunction solar cell exploiting a TiO_x layer as an electron selective contact (squares). The red line represents the fitting obtained with the model described in (8-9), whilst the blue line with circles is the extrapolation of the J-V curve obtained considering only the parameters of the heterojunction solar cell without the rectifying junction.. The oxide layer was deposited with $PO_2 = 1\times10^{-3}$ mbar at T_{amb}.

4. Conclusion

In this work, the synthesis and the characterization of amorphous titanium dioxide films have been performed to investigate its use as a selective contact in an HJT solar cell. For this purpose, thin films of sub-stoichiometric amorphous TiO_x were deposited by PLD with different deposition conditions (in terms of both oxygen pressure and substrate temperature). The surface analysis performed by XPS confirmed the composition of the films and highlighted the presence of the substoichiometric oxide. Optical spectra displayed a pronounced absorption peak in the near-infrared range associated to a small polaron, the energy positions of which remained constant independently from the deposition conditions. In contrast, the peak values decreased with the oxygen pressure during deposition. The defect area showed a similar trend as a function of both deposition temperature and pressure. From the fitting of the experimental absorption spectra, and from the polaron theory, it was found that the inter-band defect density is centered around 1 eV below the edge of the conduction band with amplitude decreasing with increasing temperature and oxygen pressure. The energy position of the defect density remained constant among the samples, highlighting that the chemical nature of the defect is the same within the samples. This result is consistent with the XPS analysis that shown the presence of sub-stoichiometric oxides in the samples. The polaron binding energy resulted approximately in 0.93 eV while the longitudinal-optical phonon energy in 85 meV. From this analysis, it was possible to obtain parameters functional to simulate TiO_x appropriately in advanced device simulators. The proposed method can be applied to other materials exhibiting similar absorption coefficients, such as transition metal oxides. By using the results from the small polaron theory, it was possible to improve an existing approach in the defects density characterization. This approach and the data are of great interest in the field of solar cells simulation. Information and analysis on the defects DOS in many materials likewise the transition metal oxides are still missing and without these data, the simulation of transition metal oxides-based solar cells may not be accurate. Indeed, for transport mechanisms such as the *trap-assisted tunneling* (which occurs in the carrier selective contact of these solar cells) rely on the defect distribution near the edge of the TMO conduction band. Therefore, the knowledge of the TiO_x defect DOS is essential to achieve the optimization of solar cells involving this TMO as electron selective contact.

The impact of TiO_x as an electron selective contact in c-Si heterojunction solar cells was successively tested by realizing a prototype with TiO_x deposited by PLD at room temperature with an oxygen pressure of 1×10^{-3} mbar. This device was then electrically characterized, exhibiting an S-shaped DC *J-V* curve. Such behavior was analyzed by implementing a previously developed model for solar cells presenting anomalous electrical characteristics. The experimental data were used to determine a quantitative parameter for the solar cell equivalent parameters. The simulated characteristics resulted in a good fit with the measured data for a broad voltage range, giving input to further optimize the TiO_x contact.

Acknowledgements

We thank A. Nicolosi for the assistance with the PLD deposition, M. Bonadonna for the assistance with the XPS analysis and Y. Zhao for the assistance with the solar cell prototype manufacturing..

References

[1] FRAUNHOFER INSTITUTE FOR SOLAR ENERGY SYSTEMS *Photovoltaics Report*; Freiburg, 2021;

[2] Green, M.; Dunlop, E.; Hohl-Ebinger, J.; Yoshita, M.; Kopidakis, N.; Hao, X. Solar Cell Efficiency Tables (Version 57). *Prog. Photovoltaics Res. Appl.* **2021**, *29*, 3–15, doi:10.1002/pip.3371.

[3] Yoshikawa, K.; Kawasaki, H.; Yoshida, W.; Irie, T.; Konishi, K.; Nakano, K.; Uto, T.; Adachi, D.; Kanematsu, M.; Uzu, H.; et al. Silicon Heterojunction Solar Cell with Interdigitated Back Contacts for a Photoconversion Efficiency over 26%. *Nat. Energy* **2017**, *2*, doi:10.1038/nenergy.2017.32.

[4] Enel Green Power New Efficiency Record for the Innovative Solar Cells Produced by 3SUN Based on Heterojunction Technology Available online: https://www.enelgreenpower.com/media/news/2020/02/3sun-solar-cell-bifacials-efficiency-record (accessed on 11 March 2021).

[5] McEvoy, A.; Markvart, T.; Castaner, L. *Practical Handbook of Photovoltaics*; 2012; ISBN 9780123859341.

[6] Holman, Z.C.; Descoeudres, A.; Barraud, L.; Fernandez, F.Z.; Seif, J.P.; De Wolf, S.; Ballif, C. Current Losses at the Front of Silicon Heterojunction Solar Cells. *IEEE J. Photovoltaics* **2012**, *2*, 7–15, doi:10.1109/JPHOTOV.2011.2174967.

[7] Bullock, J.; Hettick, M.; Geissbühler, J.; Ong, A.J.; Allen, T.; Sutter-Fella, C.M.; Chen, T.; Ota, H.; Schaler, E.W.; De Wolf, S.; et al. Efficient Silicon Solar Cells with Dopant-Free Asymmetric Heterocontacts. *Nat. Energy* **2016**, *1*, doi:10.1038/nenergy.2015.31.

[8] Melskens, J.; Van De Loo, B.W.H.; Macco, B.; Black, L.E.; Smit, S.; Kessels, W.M.M. Passivating Contacts for Crystalline Silicon Solar Cells: From Concepts and Materials to Prospects. *IEEE J. Photovoltaics* **2018**, *8*, 373–388, doi:10.1109/JPHOTOV.2018.2797106.

[9] Cho, J.; Melskens, J.; Debucquoy, M.; Recamán Payo, M.;

Jambaldinni, S.; Bearda, T.; Gordon, I.; Szlufcik, J.; Kessels, W.M.M.; Poortmans, J. Passivating Electron-Selective Contacts for Silicon Solar Cells Based on an a-Si:H/TiOx Stack and a Low Work Function Metal. *Prog. Photovoltaics Res. Appl.* **2018**, *26*, 835–845, doi:10.1002/pip.3023.

[10] Ding, J.; Zhou, Y.; Dong, G.; Liu, M.; Yu, D.; Liu, F. Solution-Processed ZnO as the Efficient Passivation and Electron Selective Layer of Silicon Solar Cells. *Prog. Photovoltaics Res. Appl.* **2018**, *26*, doi:10.1002/pip.3044.

[11] Yang, X.; Aydin, E.; Xu, H.; Kang, J.; Hedhili, M.; Liu, W.; Wan, Y.; Peng, J.; Samundsett, C.; Cuevas, A.; et al. Tantalum Nitride Electron-Selective Contact for Crystalline Silicon Solar Cells. *Adv. Energy Mater.* **2018**, *8*, doi:10.1002/aenm.201800608.

[12] Horynová, E.; Romanyuk, O.; Horák, L.; Remeš, Z.; Conrad, B.; Peter Amalathas, A.; Landová, L.; Houdková, J.; Jiříček, P.; Finsterle, T.; et al. Optical Characterization of Low Temperature Amorphous MoOx, WOX, and VOx Prepared by Pulsed Laser Deposition. *Thin Solid Films* **2020**, *693*, doi:10.1016/j.tsf.2019.137690.

[13] Scire, D.; Bonadonna, M.; Zhao, Y.; Procel, P.; Isabella, O.; Zeman, M.; MacAluso, R.; Mosca, M.; Crupi, I. Analysis of Transition Metal Oxides Based Heterojunction Solar Cells with S-Shaped J-V Curves. In Proceedings of the 12th AEIT International Annual Conference, AEIT 2020; IEEE, September 23 2020; pp. 1–6.

[14] Messmer, C.; Bivour, M.; Schön, J.; Hermle, M. Requirements for Efficient Hole Extraction in Transition Metal Oxide-Based Silicon Heterojunction Solar Cells. *J. Appl. Phys.* **2018**, *124*, doi:10.1063/1.5045250.

[15] Gesheva, K.; Ivanova, T.; Bodurov, G.; Szilágyi, I.M.; Justh, N.; Kéri, O.; Boyadjiev, S.; Nagy, D.; Aleksandrova, M. Technologies for Deposition of Transition Metal Oxide Thin Films: Application as Functional Layers in "Smart Windows" and Photocatalytic Systems. In Proceedings of the Journal of Physics: Conference Series; 2016; Vol. 682.

[16] Mews, M.; Lemaire, A.; Korte, L. Sputtered Tungsten Oxide as Hole Contact for Silicon Heterojunction Solar Cells. *IEEE J. Photovoltaics* **2017**, *7*, 1209–1215, doi:10.1109/JPHOTOV.2017.2714193.

[17] Mallem, K.; Kim, Y.J.; Hussain, S.Q.; Dutta, S.; Le, A.H.T.; Ju, M.; Park, J.; Cho, Y.H.; Kim, Y.; Cho, E.C.; et al. Molybdenum Oxide: A Superior Hole Extraction Layer for Replacing p-Type Hydrogenated Amorphous Silicon with High Efficiency Heterojunction Si Solar Cells. *Mater. Res. Bull.* **2019**, *110*, 90–96, doi:10.1016/j.materresbull.2018.10.018.

[18] Yu, C.; Xu, S.; Yao, J.; Han, S. Recent Advances in and New Perspectives on Crystalline Silicon Solar Cells with Carrier-Selective Passivation Contacts. *Crystals* **2018**, *8*, doi:10.3390/cryst8110430.

[19] Dréon, J.; Jeangros, Q.; Cattin, J.; Haschke, J.; Antognini, L.; Ballif, C.; Boccard, M. 23.5%-Efficient Silicon Heterojunction Silicon Solar Cell Using Molybdenum Oxide As Hole-Selective Contact. *Nano Energy* **2020**, *70*, doi:10.1016/j.nanoen.2020.104495.

[20] Perego, M.; Seguini, G.; Scarel, G.; Fanciulli, M.; Wallrapp, F. Energy Band Alignment at Ti O2 Si Interface with Various Interlayers. *J. Appl. Phys.* **2008**, *103*, doi:10.1063/1.2885109.

[21] Matsui, T.; Bivour, M.; Ndione, P.F.; Bonilla, R.S.; Hermle, M. Origin of the Tunable Carrier Selectivity of Atomic-Layer-Deposited TiOx Nanolayers in Crystalline Silicon Solar Cells. *Sol. Energy Mater. Sol. Cells* **2020**, *209*, 110461, doi:10.1016/j.solmat.2020.110461.

[22] Yang, J.; Li, L.; Li, W.; Mao, L. Formation Mechanism of Conduction Path in Titanium Dioxide with Ti-Interstitials-Doped: Car-Parrinello Molecular Dynamics. In Proceedings of the AIP Conference Proceedings; 2017; Vol. 1794.

[23] Yang, X.; Bi, Q.; Ali, H.; Davis, K.; Schoenfeld, W. V.; Weber, K. High-Performance TiO2-Based Electron-Selective Contacts for Crystalline Silicon Solar Cells. *Adv. Mater.* **2016**, *28*, 5891–5897, doi:10.1002/adma.201600926.

[24] Nagamatsu, K.A.; Avasthi, S.; Sahasrabudhe, G.; Man, G.; Jhaveri, J.; Berg, A.H.; Schwartz, J.; Kahn, A.; Wagner, S.; Sturm, J.C. Titanium Dioxide/Silicon Hole-Blocking Selective Contact to Enable Double-Heterojunction Crystalline Silicon-Based Solar Cell. *Appl. Phys. Lett.* **2015**, *106*, doi:10.1063/1.4916540.

[25] Yang, X.; Weber, K.; Hameiri, Z.; De Wolf, S. Industrially Feasible, Dopant-Free, Carrier-Selective Contacts for High-Efficiency Silicon Solar Cells. *Prog. Photovoltaics Res. Appl.* **2017**, *25*, 896–904, doi:10.1002/pip.2901.

[26] Allen, T.G.; Bullock, J.; Jeangros, Q.; Samundsett, C.; Wan, Y.; Cui, J.; Hessler-Wyser, A.; De Wolf, S.; Javey, A.; Cuevas, A. A Low Resistance Calcium/Reduced Titania Passivated Contact for High Efficiency Crystalline Silicon Solar Cells. *Adv. Energy Mater.* **2017**, *7*, 1602606, doi:10.1002/aenm.201602606.

[27] Huh, D.; Oh, K.; Kim, M.; Choi, H.-J.; Kim, D.S.; Lee, H. Selectively Patterned TiO2 Nanorods as Electron Transport Pathway for High Performance Perovskite Solar Cells. *Nano Res.* **2019**, *12*, 601–606, doi:10.1007/s12274-018-2263-x.

[28] Pan, B.; Gu, J.; Xu, X.; Xiao, L.; Zhao, J.; Zou, G. Interface Engineering of High Performance All-Inorganic Perovskite Solar Cells via Low-Temperature Processed TiO2 Nanopillar Arrays. *Nano Res.* **2021**, *12*, doi:10.1007/s12274-021-3566-x.

[29] Rathee, D.; Arya, S.K.; Kumar, M. Analysis of TiO2 for Microelectronic Applications: Effect of Deposition Methods on Their Electrical Properties. *Front. Optoelectron. China* **2011**, *4*, doi:10.1007/s12200-011-0188-z.

[30] Aglieri, V.; Zaffora, A.; Lullo, G.; Santamaria, M.; Di Franco, F.; Lo Cicero, U.; Mosca, M.; Macaluso, R. Resistive Switching in Microscale Anodic Titanium Dioxide-Based Memristors. *Superlattices Microstruct.* **2018**, *113*, doi:10.1016/j.spmi.2017.10.031.

[31] Mosca, M.; Macaluso, R.; Randazzo, G.; Di Bella, M.; Caruso, F.; Cali, C.; Di Franco, F.; Santamaria, M.; Di Quarto, F. Anodized Ti-Si Alloy as Gate Oxide of Electrochemically-Fabricated Organic Field-Effect Transistors. *ECS Solid State Lett.* **2014**, *3*, P7–P9, doi:10.1149/2.007401ssl.

[32] Ji, T.; He, S.; Ai, F.; Wu, J.; Yan, L.; Hu, J.; Liao, M. An Adjustable Multi-Color Detector Based on Regulating TiO2 Surface Adsorption and Multi-Junction Synergy. *Nano Res.* **2021**, *12*, 31–36, doi:10.1007/s12274-021-3565-y.

[33] Li, Y.; Cooper, J.K.; Liu, W.; Sutter-Fella, C.M.; Amani, M.; Beeman, J.W.; Javey, A.; Ager, J.W.; Liu, Y.; Toma, F.M.; et al. Defective TiO2 with High Photoconductive Gain for Efficient and Stable Planar Heterojunction Perovskite Solar Cells. *Nat. Commun.* **2016**, *7*, doi:10.1038/ncomms12446.

[34] Lewis, A.; Troughton, J.R.; Smith, B.; McGettrick, J.; Dunlop, T.; De Rossi, F.; Pockett, A.; Spence, M.; Carnie, M.J.; Watson, T.M.; et al. In-Depth Analysis of Defects in TiO2 Compact Electron Transport Layers and Impact on Performance and Hysteresis of Planar Perovskite Devices at Low Light. *Sol. Energy Mater. Sol. Cells* **2020**, *209*, doi:10.1016/j.solmat.2020.110448.

[35] Messmer, C.; Bivour, M.; Schon, J.; Glunz, S.W.; Hermle, M. Numerical Simulation of Silicon Heterojunction Solar Cells

Featuring Metal Oxides as Carrier-Selective Contacts. *IEEE J. Photovoltaics* **2018**, *8*, 456–464, doi:10.1109/JPHOTOV.2018.2793762.

[36] Shen, H.; Omelchenko, S.T.; Jacobs, D.A.; Yalamanchili, S.; Wan, Y.; Yan, D.; Phang, P.; Duong, T.; Wu, Y.; Yin, Y.; et al. In Situ Recombination Junction between P-Si and TiO 2 Enables High-Efficiency Monolithic Perovskite/Si Tandem Cells. *Sci. Adv.* **2018**, *4*, eaau9711, doi:10.1126/sciadv.aau9711.

[37] Vaněček, M.; Kočka, J.; Stuchlík, J.; Kožíšek, Z.; Štika, O.; Tříska, A. Density of the Gap States in Undoped and Doped Glow Discharge A-Si:H. *Sol. Energy Mater.* **1983**, *8*, 411–423, doi:10.1016/0165-1633(83)90006-0.

[38] Kočka, J.; Vaněček, M.; Tříska, A. ENERGY AND DENSITY OF GAP STATES IN a-Si:H . In *Amorphous Silicon and Related Materials*; Frtitzsche, H., Ed.; WORLD SCIENTIFIC, 1989; pp. 297–327.

[39] Morawiec, S.; Holovský, J.; Mendes, M.J.; Müller, M.; Ganzerová, K.; Vetushka, A.; Ledinský, M.; Priolo, F.; Fejfar, A.; Crupi, I. Experimental Quantification of Useful and Parasitic Absorption of Light in Plasmon-Enhanced Thin Silicon Films for Solar Cells Application. *Sci. Rep.* **2016**, *6*, doi:10.1038/srep22481.

[40] Scirè, D.; Procel, P.; Gulino, A.; Isabella, O.; Zeman, M.; Crupi, I. Sub-Gap Defect Density Characterization of Molybdenum Oxide: An Annealing Study for Solar Cell Applications. *Nano Res.* **2020**, *13*, 3416–3424, doi:10.1007/s12274-020-3029-9.

[41] Scirè, D.; Macaluso, R.; Mosca, M.; Mirabella, S.; Gulino, A.; Isabella, O.; Zeman, M.; Crupi, I. Characterization of the Defect Density States in MoOx for C-Si Solar Cell Applications. *Solid. State. Electron.* **2021**, *185*, 108135, doi:10.1016/j.sse.2021.108135.

[42] Sherwood, P.M.A. Data Analysis in X-ray Photoelectron Spectroscopy. In *Practical surface analysis*; Briggs, D., Seah, M.P., Eds.; John Wiley and Sons: Chichester, 1990; Vol. 1.

[43] Wagner, C.D.; Davis, L.E.; Riggs, W.M. The Energy Dependence of the Electron Mean Free Path. *Surf. Interface Anal.* **1980**, *2*, doi:10.1002/sia.740020204.

[44] Naumkin, A. V; Kraust-Vass, A.; Gaarenstroom, S.W.; Powell, C.J. NIST X-Ray Photoelectron Spectroscopy Database, National Institute of Standards and Technology.

[45] Remes, Z.; Vasudevan, R.; Jarolimek, K.; Smets, A.H.M.; Zeman, M. The Optical Spectra of A-Si:H and a-SiC:H Thin Films Measured by the Absolute Photothermal Deflection Spectroscopy (PDS). *Solid State Phenom.* **2014**, *213*, 19–28, doi:10.4028/www.scientific.net/SSP.213.19.

[46] Singh, M.; Santbergen, R.; Mazzarella, L.; Madrampazakis, A.; Yang, G.; Vismara, R.; Remes, Z.; Weeber, A.; Zeman, M.; Isabella, O. Optical Characterization of Poly-SiOx and Poly-SiCx Carrier-Selective Passivating Contacts. *Sol. Energy Mater. Sol. Cells* **2020**, *210*, doi:10.1016/j.solmat.2020.110507.

[47] Zhao, Y.; Mazzarella, L.; Procel, P.; Han, C.; Yang, G.; Weeber, A.; Zeman, M.; Isabella, O. Doped Hydrogenated Nanocrystalline Silicon Oxide Layers for High-Efficiency c-Si Heterojunction Solar Cells. *Prog. Photovoltaics Res. Appl.* **2020**, *28*, 425–435, doi:10.1002/pip.3256.

[48] Bharti, B.; Kumar, S.; Lee, H.N.; Kumar, R. Formation of Oxygen Vacancies and Ti3+ State in TiO2 Thin Film and Enhanced Optical Properties by Air Plasma Treatment. *Sci. Rep.* **2016**, *6*, doi:10.1038/srep32355.

[49] Sanjinés, R.; Tang, H.; Berger, H.; Gozzo, F.; Margaritondo, G.; Lévy, F. Electronic Structure of Anatase TiO2 Oxide. *J. Appl. Phys.* **1994**, *75*, 2945–2951, doi:10.1063/1.356190.

[50] Gouttebaron, R.; Cornelissen, D.; Snyders, R.; Dauchot, J.P.; Wautelet, M.; Hecq, M. XPS Study of TiOx Thin Films Prepared by d.c. Magnetron Sputtering in Ar-O2 Gas Mixtures. *Surf. Interface Anal.* **2000**, *30*, 527–530, doi:10.1002/1096-9918(200008)30:1<527::AID-SIA834>3.0.CO;2-Z.

[51] Akl, A.A.; Kamal, H.; Abdel-Hady, K. Fabrication and Characterization of Sputtered Titanium Dioxide Films. *Appl. Surf. Sci.* **2006**, *252*, 8651–8656, doi:10.1016/j.apsusc.2005.12.001.

[52] Zhang, J.Y.; Boyd, I.W.; O'Sullivan, B.J.; Hurley, P.K.; Kelly, P. V.; Sénateur, J.P. Nanocrystalline TiO2 Films Studied by Optical, XRD and FTIR Spectroscopy. *J. Non. Cryst. Solids* **2002**, *303*, 134–138, doi:10.1016/S0022-3093(02)00973-0.

[53] Katagiri, K.; Suzuki, T.; Muto, H.; Sakai, M.; Matsuda, A. Low Temperature Crystallization of TiO2 in Layer-by-Layer Assembled Thin Films Formed from Water-Soluble Ti-Complex and Polycations. *Colloids Surfaces A Physicochem. Eng. Asp.* **2008**, *321*, 233–237, doi:10.1016/j.colsurfa.2007.11.028.

[54] Matthews, A. The Crystallization of Anatase and Rutile from Amorphous Titanium Dioxide under Hydrothermal Conditions. *Am. Mineral.* **1976**, *61*, 419–424.

[55] Bakri, A.S.; Sahdan, M.Z.; Adriyanto, F.; Raship, N.A.; Said, N.D.M.; Abdullah, S.A.; Rahim, M.S. Effect of Annealing Temperature of Titanium Dioxide Thin Films on Structural and Electrical Properties. In Proceedings of the AIP Conference Proceedings; 2017; Vol. 1788.

[56] Zhang, Q.; Ma, L.; Shao, M.; Huang, J.; Ding, M.; Deng, X.; Wei, X.; Xu, X. Anodic Oxidation Synthesis of One-Dimensional TiO2 Nanostructures for Photocatalytic and Field Emission Properties. *J. Nanomater.* 2014, *2014*.

[57] Stagi, L.; Carbonaro, C.M.; Corpino, R.; Chiriu, D.; Ricci, P.C. Light Induced TiO2 Phase Transformation: Correlation with Luminescent Surface Defects. *Phys. Status Solidi Basic Res.* **2015**, *252*, 124–129, doi:10.1002/pssb.201400080.

[58] Rajaraman, T.S.; Parikh, S.P.; Gandhi, V.G. Black TiO2: A Review of Its Properties and Conflicting Trends. *Chem. Eng. J.* 2020, *389*, 123918.

[59] Zhu, G.; Ma, L.; Lin, H.; Zhao, P.; Wang, L.; Hu, Y.; Chen, R.; Chen, T.; Wang, Y.; Tie, Z.; et al. High-Performance Li-Ion Capacitor Based on Black-TiO2-x/Graphene Aerogel Anode and Biomass-Derived Microporous Carbon Cathode. *Nano Res.* **2019**, *12*, 1713–1719, doi:10.1007/s12274-019-2427-3.

[60] Daniel, L.S.; Nagai, H.; Yoshida, N.; Sato, M. Photocatalytic Activity of Vis-Responsive Ag-Nanoparticles/TiO2 Composite Thin Films Fabricated by Molecular Precursor Method (MPM). *Catalysts* **2013**, *3*, 625–645, doi:10.3390/catal3030625.

[61] Koster, G.; Blank, D.H.A.; Rijnders, G.A.J.H.M. Oxygen in Complex Oxide Thin Films Grown by Pulsed Laser Deposition: A Perspective. *J. Supercond. Nov. Magn.* **2020**, *33*, 205–212, doi:10.1007/s10948-019-05276-5.

[62] Tauc, J.; Grigorovici, R.; Vancu, A. Optical Properties and Electronic Structure of Amorphous Germanium. *Phys. Status Solidi* **1966**, *15*, 627–637, doi:10.1002/pssb.19660150224.

[63] Urbach, F. The Long-Wavelength Edge of Photographic Sensitivity and of the Electronic Absorption of Solids [8]. *Phys. Rev.* 1953, *92*.

[64] Zhong, Q.; Vohs, J.M.; Bonnell, D.A. Effect of Reduction on the Topographic and Electronic Structure of TiO2(110) Surfaces. *Surf. Sci.* **1992**, *274*, 35–43, doi:10.1016/0039-6028(92)90097-P.

[65] Choudhury, B.; Choudhury, A. Oxygen Defect Dependent Variation of Band Gap, Urbach Energy and Luminescence Property of Anatase, Anatase-Rutile Mixed Phase and of Rutile Phases of TiO2

Nanoparticles. *Phys. E Low-Dimensional Syst. Nanostructures* **2014**, *56*, 364–371, doi:10.1016/j.physe.2013.10.014.

[66] Bouizem, Y.; Belfedal, A.; Sib, J.D.; Chahed, L. Density of States in Hydrogenated Amorphous Germanium Seen via Optical Absorption Spectra. *Solid State Commun.* **2003**, *126*, 675–680, doi:10.1016/S0038-1098(03)00271-0.

[67] Kormann, C.; Bahnemann, D.W.; Hoffmann, M.R. Preparation and Characterization of Quantum-Size Titanium Dioxide. *J. Phys. Chem.* **1988**, *92*, 5196–5201, doi:10.1021/j100329a027.

[68] Jackson, W.B.; Kelso, S.M.; Tsai, C.C.; Allen, J.W.; Oh, S.J. Energy Dependence of the Optical Matrix Element in Hydrogenated Amorphous and Crystalline Silicon. *Phys. Rev. B* **1985**, *31*, 5187–5198, doi:10.1103/PhysRevB.31.5187.

[69] Gulino, A.; Tabbì, G. CdO Thin Films: A Study of Their Electronic Structure by Electron Spin Resonance Spectroscopy. *Appl. Surf. Sci.* **2005**, *245*, 322–327, doi:10.1016/j.apsusc.2004.10.026.

[70] Deb, S.K.; Chopoorian, J.A. Optical Properties and Color-Center Formation in Thin Films of Molybdenum Trioxide. *J. Appl. Phys.* **1966**, *37*, 4818–4825, doi:10.1063/1.1708145.

[71] Ederth, J.; Hoel, A.; Niklasson, G.A.; Granqvist, C.G. Small Polaron Formation in Porous WO3-x Nanoparticle Films. *J. Appl. Phys.* **2004**, *96*, 5722–5726, doi:10.1063/1.1804617.

[72] Niklasson, G.A.; Klasson, J.; Olsson, E. Polaron Absorption in Tungsten Oxide Nanoparticle Aggregates. *Electrochim. Acta* **2001**, *46*, 1967–1971, doi:10.1016/S0013-4686(01)00388-7.

[73] Dieterle, M.; Weinberg, G.; Mestl, G. Raman Spectroscopy of Molybdenum Oxides - Part I. Structural Characterization of Oxygen Defects in MoO3-x by DR UV/VIS, Raman Spectroscopy and X-Ray Diffraction. *Phys. Chem. Chem. Phys.* **2002**, *4*, 812–821, doi:10.1039/b107012f.

[74] Chen, J.; Bogdanov, N.A.; Usvyat, D.; Fang, W.; Michaelides, A.; Alavi, A. The Color Center Singlet State of Oxygen Vacancies in TiO2. *J. Chem. Phys.* **2020**, *153*, doi:10.1063/5.0030658.

[75] Reticcioli, M. Polarons in Transition-Metal Oxides. In: Andreoni W., Yip S. (eds) Handbook of Materials Modeling. Springer, Cham. https://doi.org/10.1007/978-3-319-50257-1_52-1.

[76] Moses, P.G.; Janotti, A.; Franchini, C.; Kresse, G.; Van De Walle, C.G. Donor Defects and Small Polarons on the TiO2(110) Surface. *J. Appl. Phys.* **2016**, *119*, doi:10.1063/1.4948239.

[77] Colton, R.J.; Guzman, A.M.; Rabalais, J.W. Photochromism and Electrochromism in Amorphous Transition Metal Oxide Films. *Acc. Chem. Res.* **1978**, *11*, 170–176, doi:10.1021/ar50124a008.

[78] Austin, I.G.; Mott, N.F. Polarons in Crystalline and Non-Crystalline Materials. *Adv. Phys.* **2001**, *50*, 757–812, doi:10.1080/00018730110103249.

[79] Zaynobidinov, S.; Ikramov, R.G.; Jalalov, R.M. Urbach Energy and the Tails of the Density of States in Amorphous Semiconductors. *J. Appl. Spectrosc.* **2011**, *78*, 223–227, doi:10.1007/s10812-011-9450-9.

[80] Nakano, Y.; Morikawa, T.; Ohwaki, T.; Taga, Y. Origin of Visible-Light Sensitivity in N-Doped TiO2 Films. *Chem. Phys.* **2007**, *339*, 20–26, doi:10.1016/j.chemphys.2007.05.031.

[81] Freysoldt, C.; Grabowski, B.; Hickel, T.; Neugebauer, J.; Kresse, G.; Janotti, A.; Van de Walle, C.G. First-Principles Calculations for Point Defects in Solids. *Rev. Mod. Phys.* **2014**, *86*, 253–305, doi:10.1103/RevModPhys.86.253.

[82] Umebayashi, T.; Yamaki, T.; Itoh, H.; Asai, K. Analysis of Electronic Structures of 3d Transition Metal-Doped TiO2 Based on Band Calculations. *J. Phys. Chem. Solids* **2002**, *63*, 1909–1920, doi:10.1016/S0022-3697(02)00177-4.

[83] Mudgal, S.; Nayak, M.; Singh, S.; Komarala, V.K. Study of Anomalous S-Shape in Current Density-Voltage Characteristics of Carrier Selective Contact Molybdenum Oxide and Amorphous Silicon Based Heterojunction Silicon Solar Cells. In Proceedings of the AIP Conference Proceedings; 2019; Vol. 2147, p. 020009.

[84] Saive, R. S-Shaped Current-Voltage Characteristics in Solar Cells: A Review. *IEEE J. Photovoltaics* **2019**, *9*, 1477–1484, doi:10.1109/JPHOTOV.2019.2930409.

[85] Di Piazza, M.C.; Luna, M.; Vitale, G. Dynamic PV Model Parameter Identification by Least-Squares Regression. *IEEE J. Photovoltaics* **2013**, *3*, 799–806, doi:10.1109/JPHOTOV.2012.2236146.

[86] García-Sánchez, F.J.; Lugo-Muñoz, D.; Muci, J.; Ortiz-Conde, A. Lumped Parameter Modeling of Organic Solar Cells' S-Shaped I-V Characteristics. *IEEE J. Photovoltaics* **2013**, *3*, 330–335, doi:10.1109/JPHOTOV.2012.2219503.

[87] Aghassi, A.; Fay, C.D.; Mozer, A. Investigation of S-Shaped Current-Voltage Characteristics in High-Performance Solution-Processed Small Molecule Bulk Heterojunction Solar Cells. *Org. Electron.* **2018**, *62*, 133–141, doi:10.1016/j.orgel.2018.07.025.

[88] Zuo, L.; Yao, J.; Li, H.; Chen, H. Assessing the Origin of the S-Shaped I-V Curve in Organic Solar Cells: An Improved Equivalent Circuit Model. *Sol. Energy Mater. Sol. Cells* **2014**, *122*, 88–93, doi:10.1016/j.solmat.2013.11.018.

[89] Corless, R.M.; Gonnet, G.H.; Hare, D.E.G.; Jeffrey, D.J.; Knuth, D.E. On the Lambert W Function. *Adv. Comput. Math.* **1996**, *5*, 329–359, doi:10.1007/bf02124750.

[90] Breitenstein, O.; Bauer, J.; Altermatt, P.P.; Ramspeck, K. Influence of Defects on Solar Cell Characteristics. *Solid State Phenom.* **2009**, *156–158*, 1–10, doi:10.4028/www.scientific.net/SSP.156-158.1.